ISSN 1029-9599, Physical Mesomechanics, 2025, Vol. 28, No. 3, pp. 366–380. © Pleiades Publishing, Ltd., 2025.
Russian Text © The Author(s), 2025, published in Fizicheskaya Mezomekhanika, 2025, Vol. 28, No. 1, pp. 97–112.

Microstructure and High-Temperature Low-Cycle Fatigue of High-Chromium Martensitic Steel with Low Nitrogen and High Boron

S. Brazhnikov[1] and A. E. Fedoseeva[1]*

[1] *Belgorod State University, Belgorod, 308015 Russia*

* *e-mail: fedoseeva@bsu.edu.ru*

Received June 17, 2024; revised June 17, 2024; accepted June 17, 2024

Abstract—In the paper, we study the influence of high-temperature low-cycle fatigue on the microstructure of a new low-nitrogen and high-boron 10% Cr steel additionally alloyed with cobalt, tungsten, molybdenum, and rhenium. After heat treatment, the lath structure of tempered troostite with a high dislocation density both within laths and at the boundaries of martensite laths is stabilized by particles of grain-boundary carbides $M_{23}C_6$ and M_6C, as well as by carbonitrides NbX uniformly distributed throughout the matrix volume. The average width of martensite laths was 380 nm, and the density of free dislocations within the laths was 1.4×10^{14} m^{-2}. As the strain amplitude increases from 0.2 to 1% during low-cycle fatigue, the number of cycles to failure decreases by ~2 orders of magnitude, while the contribution of the plastic strain component increases significantly. Maximum softening (24%) is observed at the temperature 650°C and strain amplitude 0.6% in the middle of cyclic loading. After low-cycle fatigue tests, the studied steel contains small recrystallized grains free of lattice distortions. Moreover, the lath structure begins to transform into a subgrain structure, with the lath width and subgrain size being dependent on the strain amplitude. The density of free dislocations is hardly affected by the increase in the strain amplitude compared to the initial state, while the density of dislocations at the lath boundaries decreases significantly with strain amplitude, which is due to shortening of the martensite lath boundaries. Fractography shows that oxide particles act as sources of crack initiation at both temperatures of low-cycle fatigue tests.

Keywords: heat-resistant martensitic steels, alloying, low-cycle fatigue, long-term annealing, strengthening mechanisms, structure

DOI: 10.1134/S1029959924601568

1. INTRODUCTION

High-chromium martensitic steels with low nitrogen and high boron are promising materials for the manufacture of components for boilers and steam pipelines, rotors and blades of steam turbines of thermal power units operating at temperature 600–630°C and steam pressure 25–30 MPa [1, 2]. The advantages of these materials include high creep resistance, good fracture toughness, and low thermal expansion coefficient [3, 4]. High creep resistance of high-chromium martensitic steels is governed by the nonequilibrium lath structure of tempered troostite with a high dislocation density, which is preserved under creep conditions. This is due to pinning of boundaries and dislocations by second-phase particles, such as grain-boundary carbides $M_{23}C_6$ and Laves phases, as well as MX carbonitrides uniformly distributed throughout the ferrite matrix [1]. The nitrogen content is decreased to prevent the formation of coarse Z-phase particles, which replace fine MX carbonitrides during long-term creep in the temperature range from 550 to 700°C [5, 6]. An increased boron content leads to the formation of the coherent $M_{23}(C, B)_6$ phase with low interfacial energy, which ensures a low rate of coarsening of these particles during long-term loading [5, 6].

Along with high creep resistance, steels in operation should have good resistance to cyclic loads. High-temperature cyclic loading induces two simultaneous degradation processes [7–9]: (1) surface oxidation at

temperatures above 450°C [7] and wustite (FeO oxide) formation at temperatures above 637°C [10, 11], which, together with other iron oxides, acts as a source of crack nucleation on the material surface [7]; (2) structure recovery and recrystallization, which manifest themselves in a decreased dislocation density and the formation of both subgrains and recrystallized grains due to the nonequilibrium lath structure of tempered troostite [8, 9]. Thermal activation promotes cyclic deformation, which leads to microstructural degradation. The lath structure stability can be improved by increasing the number of small second-phase particles. These can be $M_{23}(C, B)_6$ phases [12] or yttrium oxides [13, 14]. Highly stable nanosized particles act as barriers to dislocation motion, which slows down microstructural degradation. The interaction between dislocations and second-phase particles can slow down cyclic softening and reduces the softening rate, which indicates the important role of precipitation hardening during cyclic loading [15]. The initiation of microcracks on the specimen surface and their propagation into the material, which is intensified by surface oxidation, occur simultaneously with the microstructural evolution, thus promoting cyclic softening [13]. It is rather difficult to distinguish between these two contributions [13].

It was numerously reported that temperature and strain amplitude had a significant effect on cyclic softening [12, 15–20]. Thus, temperatures up to 500°C and low strain amplitudes lead to insignificant softening of the material under cyclic loads [12–14]. Under such conditions, cracks usually initiate at high-angle boundaries due to deformation incompatibility [7]. High temperatures and strain amplitudes cause an increase in the contribution of plastic deformation, which stimulates the formation of an equiaxed subgrain structure and facilitates the propagation of fatigue cracks [15–20]. Moreover, at high temperatures, consideration should be given to surface oxidation, which leads to the appearance of several sites of primary fatigue crack initiation. In this case, oxide particles act as crack initiation sources [7].

Work [12] dealt with 10% Cr steel with low nitrogen and high boron, where the main strengthening phase was $M_{23}(C, B)_6$ particles. However, the major disadvantage of this material is the low creep strength, comprising up to 1% for 100000 h [21]. This disadvantage was overcome by adding rhenium to the steel, which favorably affected the dispersion of Laves-phase particles [22]; the creep strength was improved [21]. The aim of the present study is to report on high-temperature low-cycle fatigue and the structure of Re-containing 10% Cr steel with low nitrogen and high boron.

2. MATERIAL AND METHODS

The material to be studied is a new 10% Cr martensitic steel with the chemical composition, wt %: Fe (balance)–0.13% C–0.015% B–0.001% N–9.4% Cr–3.1% Co–2.1% W–0.6% Mo–0.29% Cu–0.17% Re–0.16% V–0.05% Nb–0.2% Ni–0.1% Si–0.03% Mn–0.04% Al. The steel was cast at the SMSM LLC (Moscow) in a vacuum-induction furnace. After peeling, ingots were homogenized at a temperature of 1150°C for 16 h, followed by forging at the same temperature to square bars with the side of 50 mm and air cooling. Heat treatment of the steel included quenching from the temperature 1050°C for 1 h with subsequent tempering at 770 °C for 3 h and air cooling.

Low-cycle fatigue tests were carried out on cylindrical specimens with the gauge diameter 5 mm and gauge length 18 mm by the tension–compression scheme with the asymmetry ratio $R = -1$ at the temperatures 600 and 650°C in air with the strain amplitudes 0.2, 0.3, 0.6, 1% and frequency 0.5 Hz using an Instron 8801 testing machine. The gauge length of a specimen reduces due to the tendency of martensitic steel specimens to buckling under compression at high strain amplitudes. One specimen was tested at each strain amplitude on account of the small amount of the cast material.

Structural studies were performed using a JEOL JEM-2100 transmission electron microscope (TEM) equipped with the INCA energy dispersive spectrometer at the accelerating voltage 200 kV and a Quanta 600FEG scanning electron microscope (SEM) equipped with the electron backscatter diffraction (EBSD) analyzer. After low-cycle fatigue tests, thin foils were cut from below the fracture surface and were prepared for TEM and SEM analysis by electrolytic polishing in the 10% perchloric acid solution in acetic acid at room temperature and the voltage 25 V using a TenuPol-5 polisher. EBSD patterns were recorded from 100×80 μm^2 areas with a step of 0.2 μm in order to determine the average distance between high-angle boundaries (which corresponds to the block size) and the ratio of low-angle to high-angle boundaries. EBSD patterns were also

Table 1. Microstructural parameters of the studied 10% Cr steel after heat treatment

Average size of the original austenite grains, μm	65 ± 5
Fraction of δ ferrite, %	0
Average size of a block, μm	2.6 ± 0.3
Average width of martensite laths, nm	380 ± 30
Density of free dislocations based on TEM by Eq. (1), m^{-2}	$(1.5 \pm 0.5) \times 10^{14}$
Kernel coefficient for the nearest neighbor	0.54°
Density of free dislocations based on EBSD by Eq. (2), m^{-2}	1.5×10^{15}
Ratio of the area of lath boundaries to the material volume S_v, μm^{-1}	456 000
Average misorientation of martensite lath boundaries	2.95°
Dislocation density at lath boundaries based on EBSD by Eq. (3), m^{-2}	$(1.4 \pm 0.1) \times 10^{14}$
Fraction of high-angle/low-angle boundaries, %	52/48
Average size of $M_{23}C_6$, nm	70 ± 5
Volume fraction of $M_{23}C_6$, % (calculated using Thermo-Calc software)	2.35
Average size of M(C, N), nm	30 ± 5
Volume fraction of M(C, N), % (calculated using Thermo-Calc software)	0.054

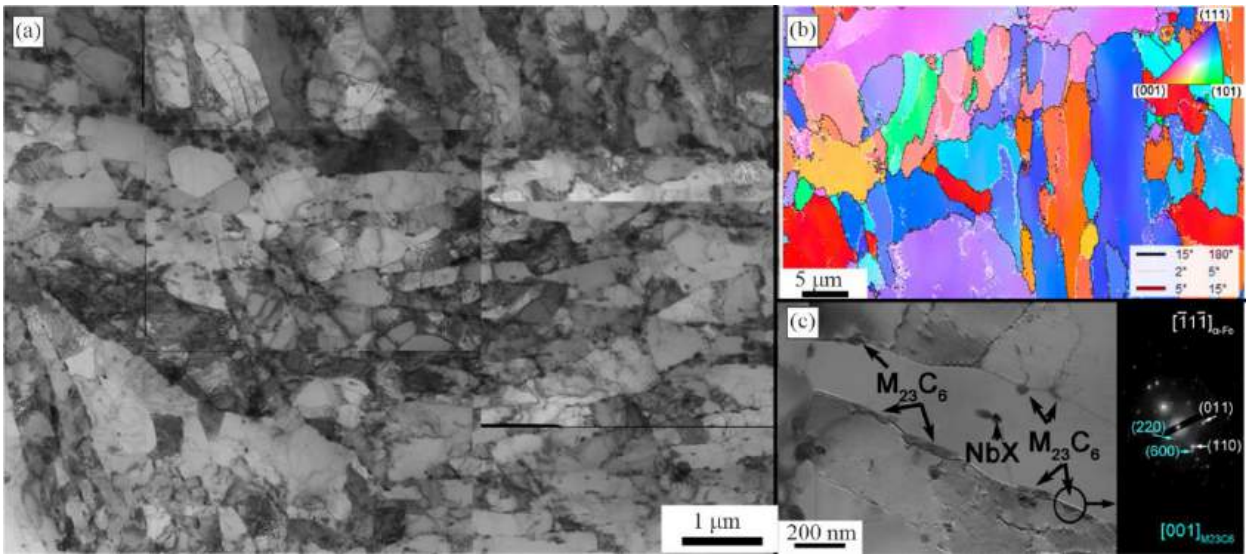

Fig. 1. TEM (a) and EBSD microstructure (b) of the studied 10% Cr steel in the initial state. Figure (c) shows images of $M_{23}C_6$ carbide particles at low-angle boundaries of martensite laths with the corresponding SAED patterns for the matrix and $M_{23}C_6$ carbide (color online).

taken from 20 × 20 μm^2 areas at a step of 0.05 μm to determine the length of low-angle boundaries misoriented to 2°–5° (which correspond to martensite lath boundaries [23, 24]), their average misorientation, the density of dislocations at the martensite lath boundaries, Kernel average misorientation (KAM, the coefficient of lattice distortion), and the density of free dislocations. The width of martensite laths and the distance between high-angle boundaries were determined by the random linear intercept method.

The density of free dislocations inside laths was estimated by the number of emergence points N on the foil surface S from TEM images [25]:

$$\rho = N/(2S). \quad (1)$$

In addition, the density of free dislocations was found by the Kernel coefficient obtained from EBSD patterns using to the expression [26]

$$\rho^* = 2\varphi/(xb), \quad (2)$$

where φ is the average Kernel coefficient taken as the average lattice distortion around each scan point for the nearest neighbor in radians, x is the scan step, and b is the Burgers vector.

The density of dislocations at martensite lath boundaries was determined from EBSD patterns by the expression [27]

$$\rho^{**} = \frac{1.5 S_v \theta}{b}, \quad (3)$$

where S_v is the ratio of the area of lath boundaries to the material volume, and θ is the average misorientation angle of lath boundaries in radians.

The particle type was determined by various methods of identification of selected-area electron diffraction (SAED) patterns and by the local chemical composition of particles using transmission electron microscopy. Volume fractions of equilibrium phases were found by mathematical modeling using Thermo-Calc software (Version 5.0.4 75) with the TCFE7 thermodynamic database. For more information on the methods refer to [3, 21, 22].

3. RESULTS AND DISCUSSION

3.1. Initial Structure after Heat Treatment

The initial microstructure of the studied 10% Cr steel after heat treatment is shown in Fig. 1 and was described in detail in [3]. The microstructural parameters after heat treatment are presented in Table 1.

In the initial state, the steel microstructure is a classical hierarchical tempered lath troostite, in which the initial austenite grains with an average size of 65 ± 5 μm are subdivided into packets, which, in turn, are subdivided into blocks with an average size of 2.6 ± 0.1 μm, which consist of martensite laths with an average width of 380 ± 30 nm (Fig. 1, Table 1). The structure contains a high dislocation density both inside laths (about 1.5×10^{14} m^{-2}) and at their boundaries (1.4×10^{14} m^{-2}) (Table 1). The dislocation densities inside laths determined by TEM (Eq. (1)) and EBSD using the Kernel coefficient (Eq. (2)) differ by an order of magnitude (Table 1). This is because the Kernel coefficient was determined for the nearest neighbors and was limited to 5°, thus including distortions not only due to dislocations, but also due to low-angle boundaries [28]. However, of our interest is the qualitative change in the Kernel coefficient and the related dislocation density after low-cycle fatigue tests rather than their quantitative values. Moreover, the dislocation densities inside laths (Eq. (1)) and at their boundaries (Eq. (3)) are in good agreement. In [29], it was stated that such a balance prevented the material from cracking.

The lath structure of tempered troostite is stabilized by $M_{23}C_6$ carbide particles, which decorate the boundaries of the original austenite grains, packets, blocks, and martensite laths (Fig. 1c) and have an average size of about 70 nm and an equilibrium volume fraction of 2.35% (Table 1). Other particles that stabilize the structure are NbX carbonitrides, which are uniformly distributed throughout the material volume (not presented here, but described in detail in [30]) and have an average size of about 30 nm and a volume fraction of 0.054% (Table 1). Note that $M_{23}C_6$ carbides located along the martensite lath boundaries demonstrate the Pitsch and Kurdyumov–Sachs orientation relationships [31] with the ferrite matrix (Fig. 1c).

3.2. Low-Cycle Fatigue at 600 and 650°C

Low-cycle fatigue tests show that increasing the strain amplitude from 0.2 to 1% significantly reduces the number of cycles to failure: by almost 2 orders of magnitude at both elevated temperatures 600 and 650°C, while a 50°C difference in the test temperature has an insignificant effect on the number of cycles (Fig. 2a). The dependence of the number of cycles on the strain amplitude in Fig. 2b shows a linear behavior with the regression slopes –0.46 at the correlation coefficient 0.965 for 600°C and–0.40 at the correlation coefficient 0.827 for 650°C (Fig. 2b).

Table 2. Low-cycle fatigue data for the studied 10% Cr steel in the middle of cyclic loading

Test temperature, °C		Strain amplitude ε_{ac}, %			
		0.2	0.3	0.6	1.0
600	$\sigma_a(N_f/2)$, MPa	235.9	274.8	309.7	322.1
	ε_{ap}, %	0.060	0.129	0.424	0.792
650	$\sigma_a(N_f/2)$, MPa	211.5	236.8	263.9	286.0
	ε_{ap}, %	0.063	0.129	0.449	0.798

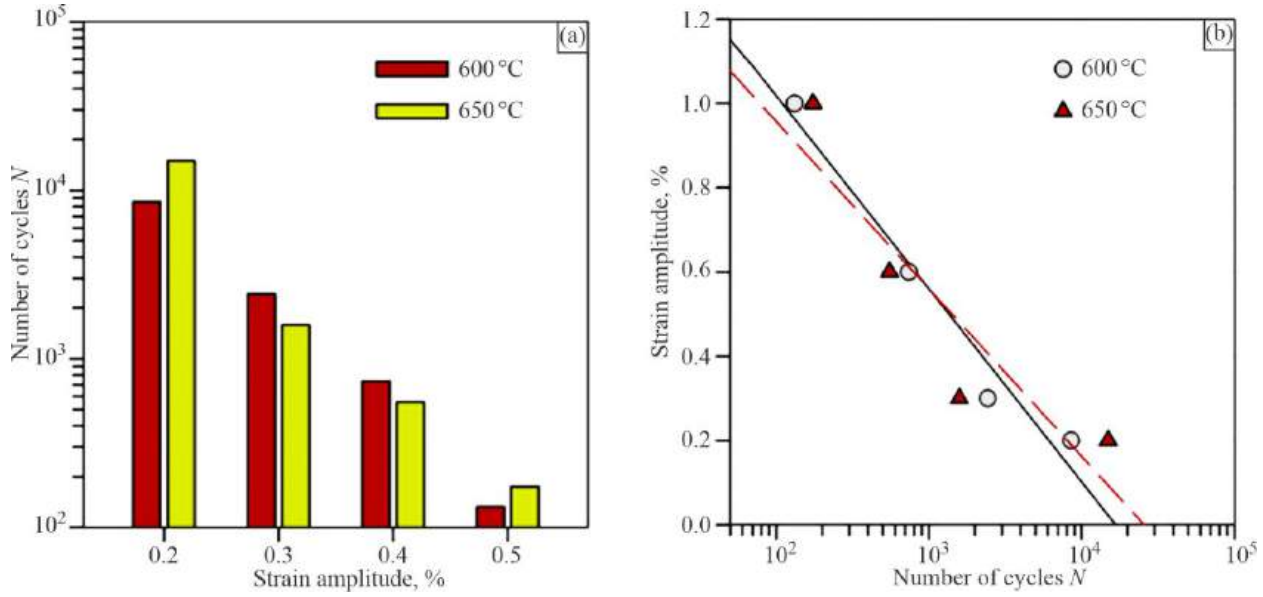

Fig. 2. Effect of the strain amplitude and test temperature on the number of cycles (color online).

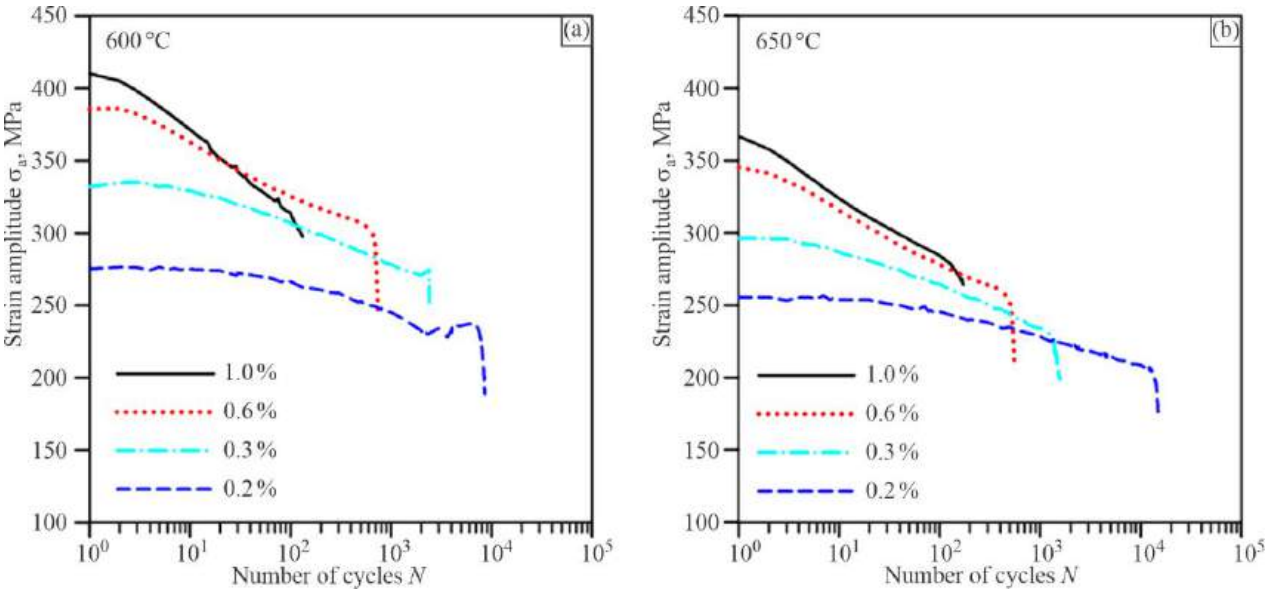

Fig. 3. Dependence of the stress amplitude on the number of cycles at the strain amplitudes 0.2, 0.3, 0.6, 1.0% and temperatures 600 (a), 650 °C (b) (color online)

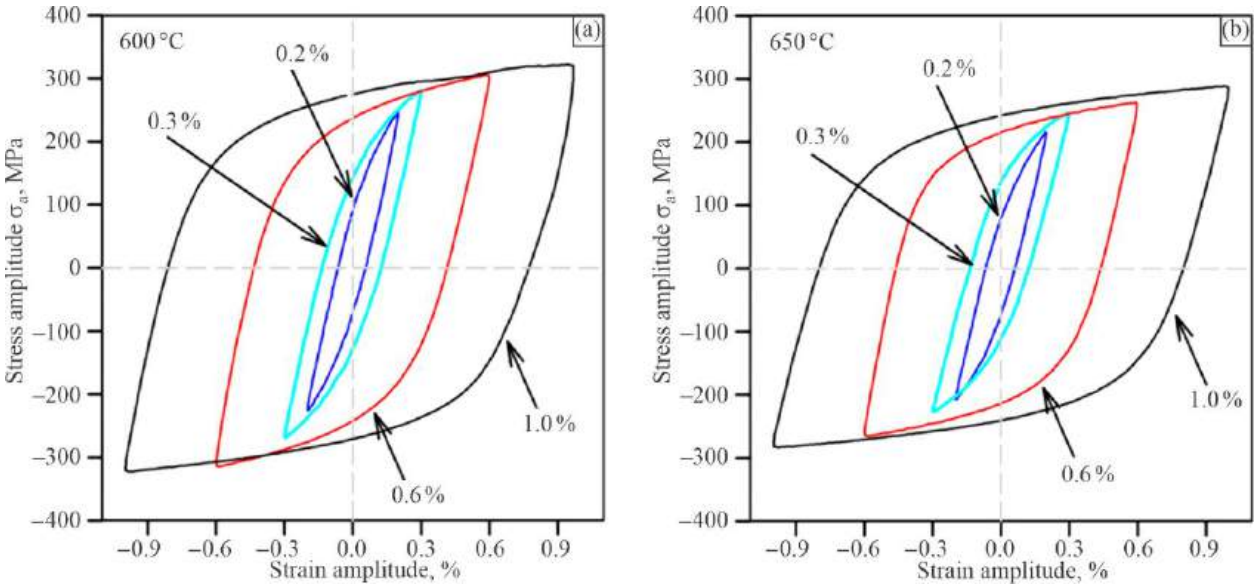

Fig. 4. Stress amplitude–strain amplitude hysteresis loops in the middle of cyclic loading at the test temperatures 600 (a) and 650°C (b) (color online).

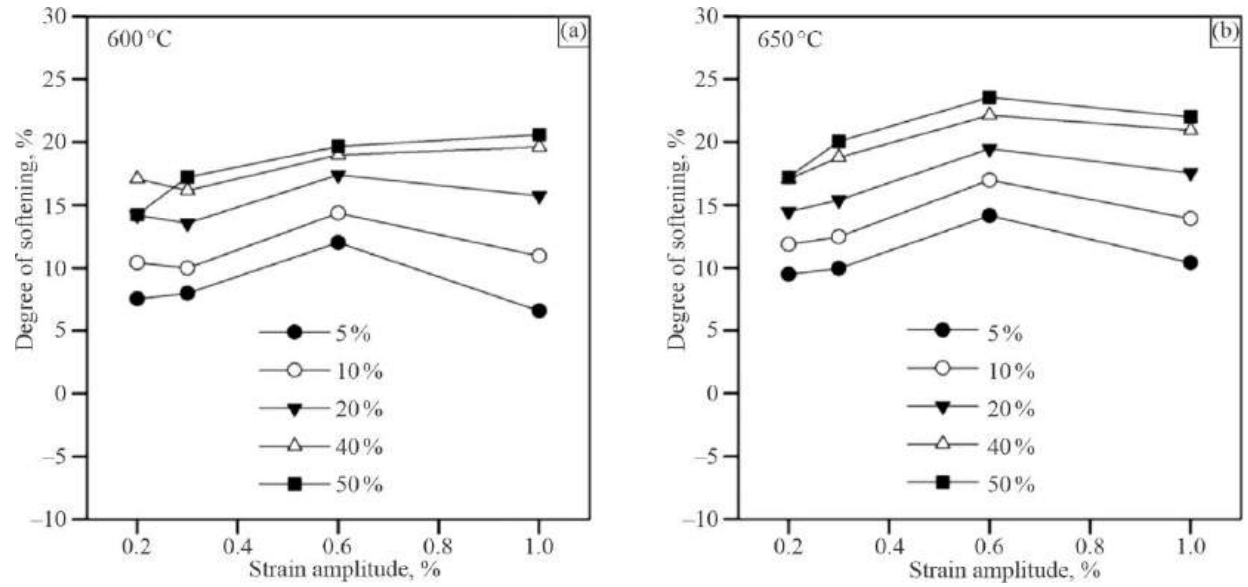

Fig. 5. Cyclic softening depending on the stress of the first cycle at different fractions of the cycle at the test temperatures 600 (a) and 650°C (b).

The dependences of the stress amplitude on the number of cycles obtained at both temperatures are shown in Fig. 3. Traditionally, the following stages are distinguished in high-chromium steels: cyclic hardening (increase in stress) and cyclic softening (decrease in stress) [12–20]. In the steel under study, no cyclic hardening stage is detected at both temperatures or all strain amplitudes (Fig. 3). From the first cycles and on, the steel demonstrates a monotonic decrease in the stress amplitude until the specimens fail. In the literature [12, 13], the absence of hardening at high temperatures is attributed to thermal recovery of the lath structure of tempered troostite and a decrease in the density of free dislocations due to their rearrangement and annihilation.

Hysteresis loops have a similar shape at both test temperatures (Fig. 4). Hysteresis loops recorded in low-cycle fatigue tests are asymmetric. They widen with strain amplitude, which is caused by an increase in the contribution of the plastic strain component. At both test temperatures, the stress amplitude and the contribution of the plastic strain component ε_{ap} in the middle of cyclic loading increase with strain amplitude (Table 2).

Table 3. Microstructural parameters of the studied 10% Cr steel after low-cycle fatigue tests

Temperature, °C	600		650			
Strain amplitude, %	0.2	0.6	0.2	0.3	0.6	1
Number of cycles N	8548	739	14927	1528	552	174
Test time, h	4.75	0.40	8.3	0.87	0.3	0.1
Distance between high-angle boundaries, μm	2.6 ± 0.3	2.1 ± 0.3	2.8 ± 0.3	2.4 ± 0.3	2.0 ± 0.3	2.3 ± 0.3
Average width of martensite laths, nm	350 ± 30	730 ± 30	570 ± 30	450 ± 30	900 ± 30	380 ± 30
Average size of subgrains, nm	470 ± 30	1150 ± 30	620 ± 30	590 ± 30	1175 ± 30	766 ± 30
Density of free dislocations based on TEM by Eq. (1), $\times 10^{14}$ m^{-2}	2.7 ± 0.5	1.6 ± 0.5	1.0 ± 0.5	1.6 ± 0.5	1.2 ± 0.5	1.4 ± 0.5
Kernel coefficient for the nearest neighbor	0.42°	0.41°	0.54°	0.45°	0.44°	0.45°
Density of free dislocations based on EBSD by Eq. (2), $\times 10^{15}$ m^{-2}	1.2	1.2	1.5	1.3	1.3	1.3
Ratio of the area of lath boundaries to the material volume S_v, μm^{-1}	294100	230800	435000	240325	294100	246950
Average misorientation of martensite lath boundaries	3.08°	3.03°	2.77°	2.95°	3.03°	2.95°
Dislocation density at lath boundaries based on EBSD by Eq. (3), $\times 10^{13}$ m^{-2}	9.6 ± 0.1	7.4 ± 0.1	13.0 ± 0.1	7.5 ± 0.1	9.4 ± 0.1	7.7 ± 0.1
Fraction of high-angle/low-angle boundaries, %	63/37	57/43	57/43	57/43	59/41	60/40

Thus, at 600 and 650°C, as the strain amplitude grows from 0.2 to 1%, the stress amplitude increment is ~30%, while the contribution of the plastic strain component increases by ~13 times (Fig. 4, Table 2).

With test temperature, the stress amplitude in the middle of cyclic loading decreases by 11–17% regardless of the strain amplitude (Table 2). At 600 and 650°C, the contribution of the plastic strain component has similar values at the same strain amplitudes (Table 2).

Figure 5 shows the degree of cyclic softening depending on the stress of the first cycle at different fractions of the cycle for both test temperatures. At 600 and 650°C, softening begins at the 5% cycle fraction and varies from 6 to 14% (Fig. 5). In the middle of cyclic loading, the softening degree varies from 14 to 24% at different strain amplitudes (Fig. 5).

At the temperature 600°C and strain amplitudes 0.2 and 0.3%, the degree of softening increases from 7 to 17% as the cycle fraction grows from 5 to 50% (Fig. 5a). At the temperature 600°C and strain amplitude 0.6%, the maximum softening is observed up to the 20% cycle fraction, after which the maximum degrees of softening are revealed at the strain amplitude 1% (Fig. 5a). The maximum softening at 600°C is 21% and corresponds to the middle of cyclic loading (Fig. 5a). At the temperature 650°C and strain amplitudes 0.2 and 0.3%, the degree of softening increases from 10 to 20% as the cycle fraction increases from 5 to 50% (Fig. 5b). At the temperature 650°C and strain amplitude 0.6%, softening is maximum at all cycle fractions compared to other strain amplitudes (Fig. 5b), varying from 14% at the 5% cycle fraction to 24% in the middle of cyclic loading (Fig. 5b). The maximum softening of 24% at 650°C occurs at the strain amplitude 0.6% in the middle of cyclic loading (Fig. 5b).

Thus, an increase in the strain amplitude significantly reduces the low-cycle fatigue strength due to a growth in the plastic strain component and softening of the material, while the temperatures 600 and 650°C are close enough to ensure similar processes of structure degradation during cyclic loading.

Microstructures formed after low-cycle fatigue tests at 600 and 650°C and different strain amplitudes are shown in Figs. 6 and 7. Table 3 summarizes microstructural parameters of the 10% Cr steel after low-cycle fatigue testing.

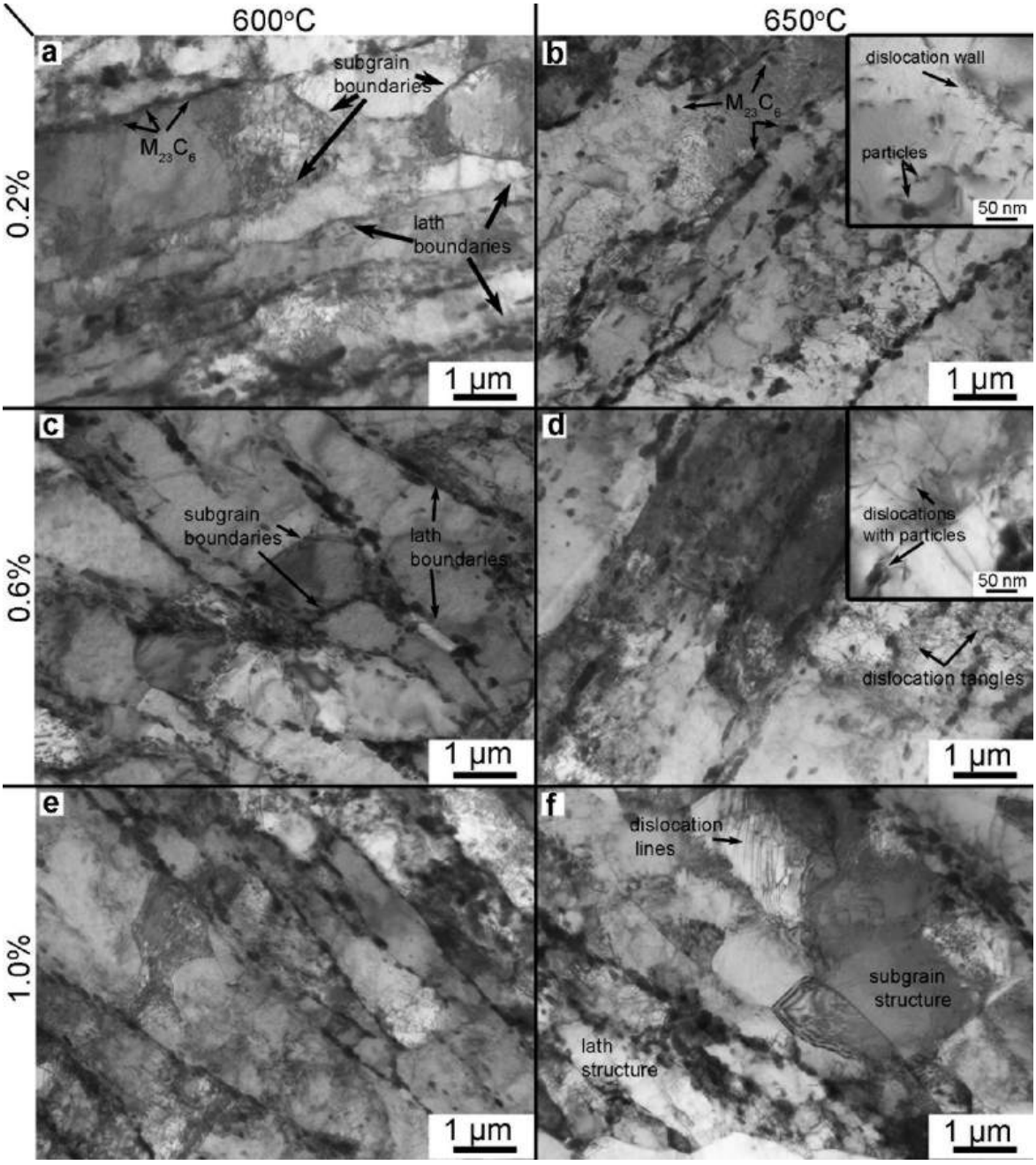

Fig. 6. Microstructure of the studied 10% Cr steel after low-cycle fatigue at the temperatures 600 (a, c, e), 650°C (b, d, f) and strain amplitudes 0.2 (a, b), 0.6 (c, d), 1% (e, f). Transmission electron microscopy.

3.3. Structure after Low-Cycle Fatigue at 600 and 650°C

From Figs. 6 and 7, as well as from Table 3, it is clear that high-temperature low-cycle fatigue has a significant effect on the lath structure of tempered troostite. At both temperatures, regardless of the strain amplitude, changes occur in the subgrain and dislocation structures, while second-phase particles and the solid solution of the ferrite matrix hardly evolve. This is explained by the fact that the evolution of particles and solid solution of the ferrite matrix is determined by both temperature and time. The longest time of low-cycle fatigue tests was 4.75 h at 600°C and 8.3 h at 650°C (Table 2), which led neither to changes in the dispersion of the existing $M_{23}C_6$ carbides and NbX carbonitrides nor to the appearance of new particles of the Laves phase (Fe_2(W, Mo)). On the contrary, the evolution of the subgrain and dislocation structures is determined by stress and temperature. Under all low-cycle fatigue conditions, martensite laths widen with the simultaneous formation of new subgrains.

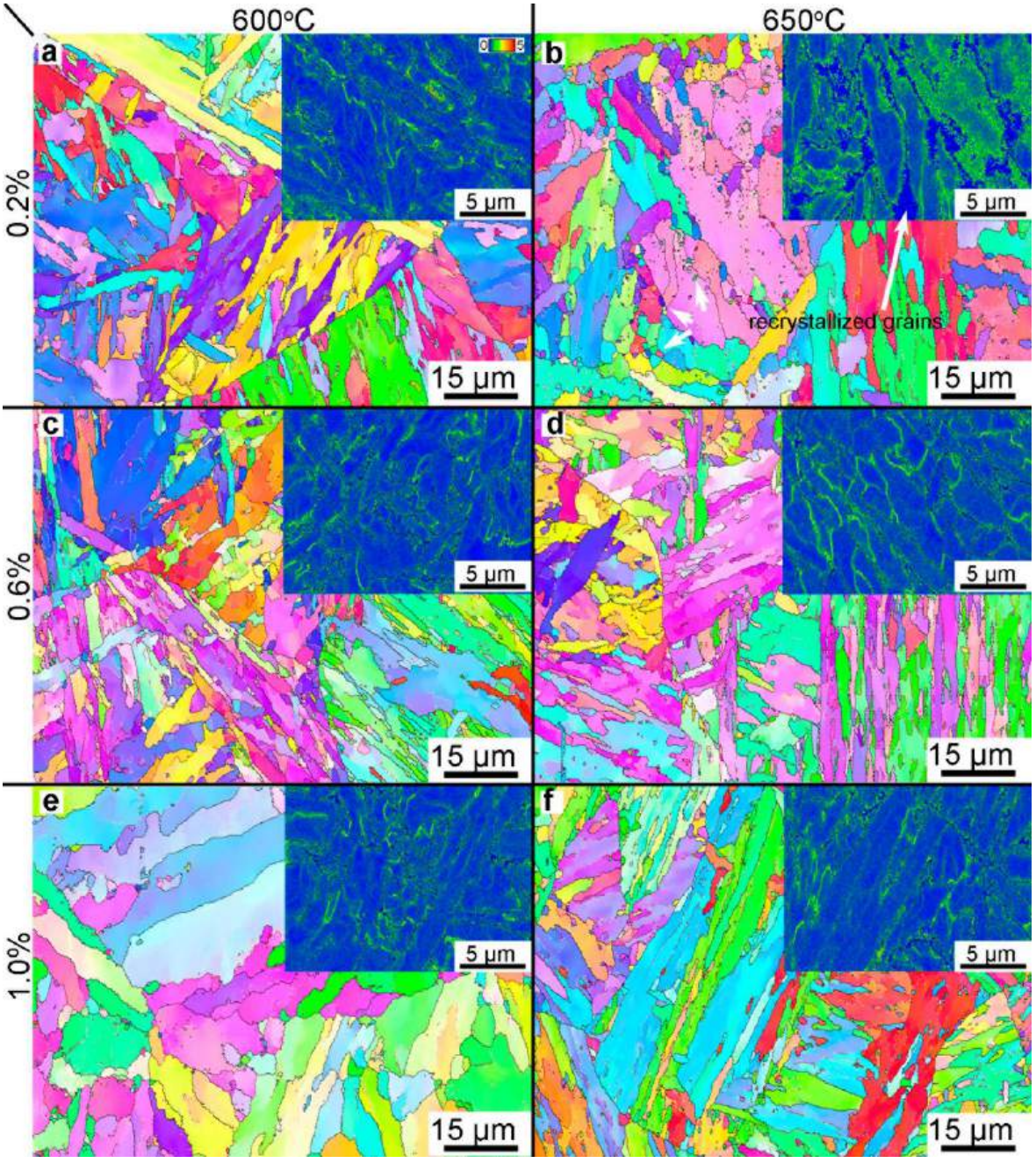

Fig. 7. EBSD microstructure of the studied 10% Cr steel after low-cycle fatigue at the temperatures 600 (a, c, e), 650°C (b, d, f) and strain amplitudes 0.2 (a, b), 0.6 (c, d), 1% (e, f). Boundaries misoriented to 2–5° are shown in pink; to 5–15°, in dark red; to 15–180°, in black. Kernel coefficients corresponding to the degree of lattice distortion are given in the upper right corner of Fig. a, varying from blue (zero lattice distortion) to red (maximum lattice distortion) (color online).

Figure 8 illustrates changes in the average sizes of a block and martensite laths as well as in the ratio of low-angle to high-angle boundaries.

At low strain amplitudes (0.2 and 0.3%), the amplitude of the plastic component does not exceed 40% of the total strain (Table 2), and stresses are close to the yield stress [3]. The fraction of high-angle boundaries increases significantly: from 52% in the initial state to 63 and 57% after low-cycle fatigue tests at 600 and 650°C, respectively, with a simultaneous decrease in the fraction of low-angle boundaries (Fig. 8b, Table 3). The average distance between high-angle boundaries remains to be 2.6 ± 0.3 μm within the measurement accuracy at both temperatures (Fig. 8a, Table 3). However, the EBSD patterns (Figs. 7a, 7b), especially the KAM

images, reveal the presence of small recrystallized grains, which are characterized by the absence of lattice distortions (marked in blue in the KAM images). Such grains are detected at both temperatures, but at 650°C, the number of recrystallized grains is higher. Moreover, the analysis of lattice distortion through the Kernel coefficient of the image shows (Figs. 7a, 7b) that the main lattice distortions (indicated in green) correspond to high-angle boundaries. In this case, the Kernel coefficient decreases from 0.54° in the initial state to 0.42°–0.45° after the low-cycle fatigue test at low strain amplitudes (Table 3). The average lath width increases to (450...550) ± 30 nm at both temperatures, while new subgrains with the average sizes of 470 ± 30 and 600 ± 30 nm are formed at 600 and 650°C, respectively (Figs. 6a, 6b, Table 3). Not all new subgrain boundaries can be detected by EBSD analysis on account of its limitation to boundaries misoriented to less than 2°. As can be seen from Figs. 6a and 6b, dislocation boundaries of the new subgrains are "loose", which bears witness to their low misorientation. The density of free dislocations inside laths decreases insignificantly, while the density of dislocations at the lath boundaries reduces to 10^{13} m^{-2} due to shortening of low-angle boundaries (Table 3). It is found that a decrease in the density of free dislocations leads to an increase in the mean free path of dislocations, which reduces the material resistance to deformation [7]. At high temperatures, dislocations are more mobile due to thermal activation, which facilitates their rearrangement and annihilation and can be accompanied by substructural transitions, which ultimately decreases the dislocation density [13, 14, 17–19].

Under high stresses of 0.6 and 1%, the plastic strain amplitude exceeds 70% of the total strain, and stresses exceed the ultimate strength of the steel [3]. The fraction of high-angle boundaries increases to 60% due to a decrease in the fraction of martensite lath boundaries with misorientation angles of up to 5° (Fig. 8b, Table 3). The average distance between high-angle boundaries decreases to 2.0 ± 0.3 μm after low-cycle fatigue at 0.6% and both temperatures (Table 3), which is caused by the formation of a large number of small recrystallized grains along high-angle boundaries (Figs. 7c, 7d). At the same time, the Kernel coefficient does not decrease below 0.41° at both temperatures (Table 3), which is comparable with the Kernel coefficient at low strain amplitudes. High-angle boundaries remain the main sources of the greatest lattice distortions (Figs. 7c–7f). As the strain amplitude grows to 1%, the distance between high-angle boundaries increases by 2 times at 600°C and by 15% at 650°C (Fig. 8), which is caused by the intensification of recrystallization processes. The average width of martensite laths increases by 1.9 and 2.4 times after low-cycle fatigue at 0.6% and the temperatures 600 and 650°C, respectively, compared to the initial structure (Figs. 6c, 6d and Tables 1, 3). Moreover, elongated subgrains with an average size of 1.15 ± 0.03 μm are found after testing at both temperatures. Low-cycle fatigue at 1% and 650°C generates a mixed structure, including the lath structure of tempered troostite with the average width of martensite laths 380 ± 30 nm (as in the initial structure) and a pronounced subgrain structure with the average subgrain size of 0.75 ± 0.03 μm (Fig. 6f, Table 3). Numerous dislocation lines and dislocation tangles are generated to compensate for plastic deformation during cyclic deformation at high strain amplitudes. This leads to the fact that the density of free dislocations inside laths remains at the same level as in the initial structure. This can explain the same Kernel coefficient after low-cycle fatigue tests at high strain amplitudes as after tests at low strain amplitudes (Table 3). However, the length of low-angle boundaries decreases with strain amplitude at both temperatures, which leads to a decrease in the dislocation density at the lath boundaries (Table 3).

3.4. Fractographic Analysis after Low-Cycle Fatigue at 600 and 650°C

Figure 9 shows fracture surfaces of the studied 10% Cr steel specimens after low-cycle fatigue tests at the temperature 650°C and the low (0.2%) and high strain amplitudes (0.6%).

The relative contraction of specimens after low-cycle fatigue significantly increases from 5 to 35% as the strain amplitude grows from 0.2 to 1% at the temperature 600°C and from 5 to 20% at the temperature 650°C. The increase in the relative contraction of the specimens is caused by an increase in the plastic strain component (Table 2).

Two zones are pronounced on the fracture surface: the fatigue fracture zone and the final fracture zone (Fig. 9). At both temperatures and all strain amplitudes, several crack initiation sites are identified, which was also found in [7]. Numerous crack initiation sites are characteristic of high-temperature tests. The fatigue fracture zone includes fatigue striations and secondary cracks as branches of the main fatigue cracks. The final fracture zone has a ductile pattern characterized by dimples.

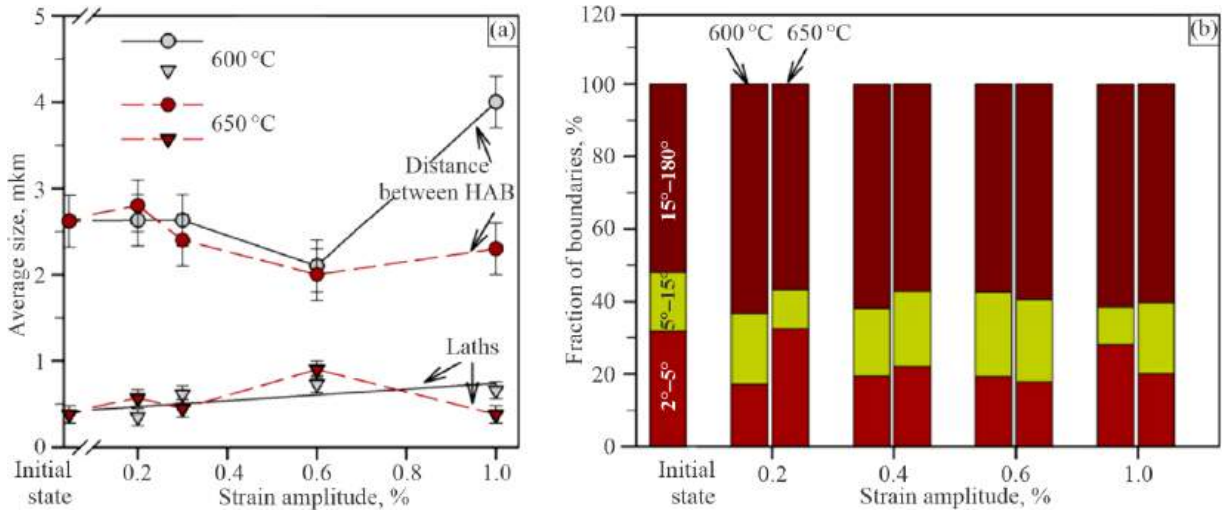

Fig. 8. Effect of temperature and strain amplitude during low-cycle fatigue on the average sizes of a block and martensite laths (a) as well as on the ratio of low-angle to high-angle boundaries (HAB) (b) (color online).

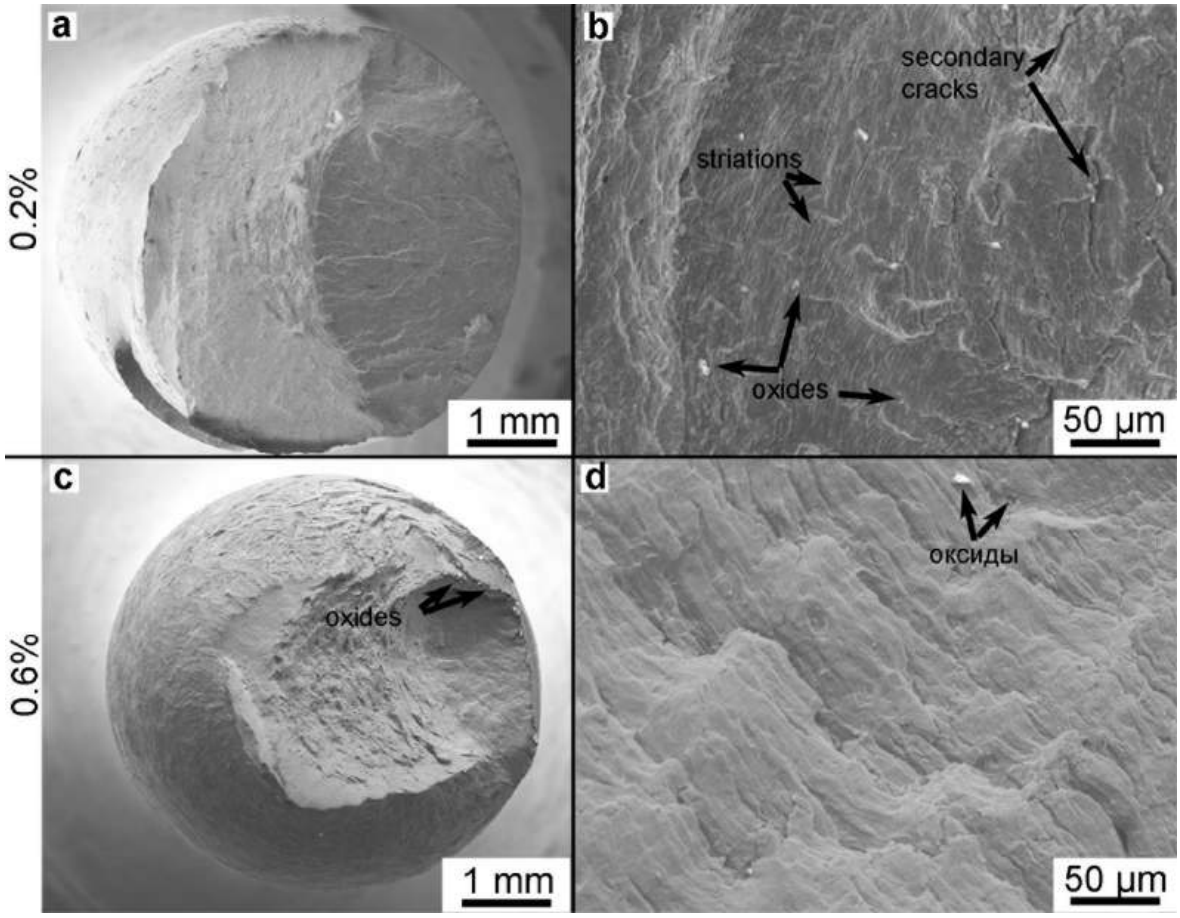

Fig. 9. Fractography of the 10% Cr steel specimens after low-cycle fatigue tests at the temperature 650°C and strain amplitudes 0.2 (a, b) and 0.6% (c, d) (color online).

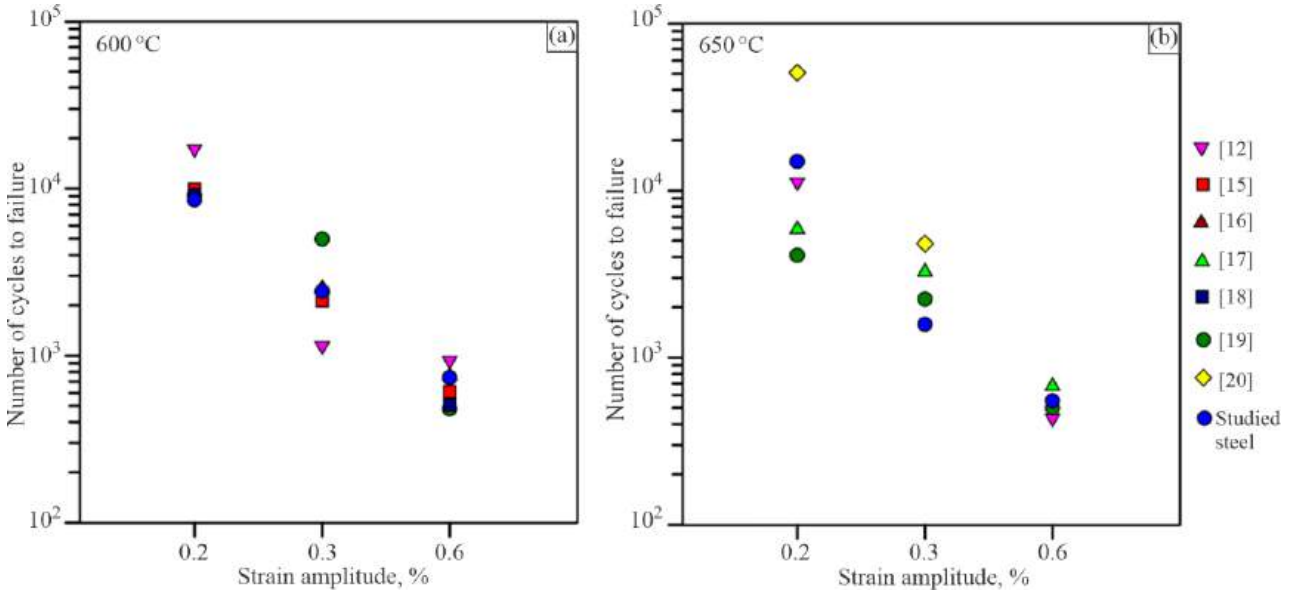

Fig. 10. Comparison of the number of cycles to failure under low-cycle fatigue of the studied 10% Cr steel with those of other 9–10% Cr steels [12, 15–20] at the temperatures 600 (a), 650°C (b) and strain amplitudes 0.2, 0.3, 0.6% (color online).

The fraction of the fatigue fracture zone on the entire fracture surface is estimated to depend significantly on the strain amplitude. It increases from 35% at the strain amplitude 0.2% to 50% at the strain amplitude 1% at the temperature 600°C and from 18% at the strain amplitude 0.2% to 43% at the strain amplitude 1% at the temperature 650°C (Figs. 9a, 9c).

The influence of surface oxidation above 450°C was shown in [7–9, 14]. Figure 9 shows oxide particles that are distributed either uniformly on the fracture surface at low strain amplitudes or on the edge of the fracture surface at high strain amplitudes. It was suggested in [7, 14] that oxide particles increased the surface roughness of the specimen during testing and could migrate deep into the material along slip bands during loading and unloading, facilitating crack propagation. On the other hand, brittle surface oxides can also induce and maintain the deformation-induced decohesion due to the wedge effect [14]. It is known that grain boundaries and slip bands are preferential sites for oxide formation. The formation of oxide layers at these sites inevitably promotes early crack initiation due to their brittleness. Moreover, Fig. 9c shows a "necklace" of oxide particles on the edge of the fracture surface at the crack initiation sites, while oxides themselves are significantly larger than those on the fracture surface at low strain amplitude (Figs. 9a, 9b). Obviously, oxides at high test temperatures are sources of crack initiation during low-cycle fatigue.

3.5. Comparison of the Low-Cycle Fatigue Properties Derived for the Steel with the Literature Data

The results obtained after low-cycle fatigue tests at 600 and 650°C in the range of strain amplitudes from 0.2 to 1% show that the number of cycles to failure of specimens of the new 10% Cr steel is close those of other high-chromium steels [12, 15–20] under equal low-cycle fatigue conditions (Fig. 10).

From Fig. 10, it is evident that, at both temperatures, the number of cycles to failure of the studied low-nitrogen high-boron 10% Cr steel additionally alloyed with cobalt, tungsten, molybdenum, copper, and rhenium is comparable with those of other 9–10% Cr–3% Co martensitic steels alloyed by different schemes. Comparison of the number of cycles to failure of the studied 10% Cr–3% Co–0.2% Re steel with those of other 9–10% Cr–3% Co steels reveals the following features.

(i) At 600°C, the studied steel demonstrates the same number of cycles to failure compared to high-nitrogen high-boron 9% Cr steels free of cobalt and rhenium [15–19], regardless of the strain amplitude. At 650°C, the studied steel demonstrates an increase in the number of cycles to failure by 2.5 and 2.0 times at the strain amplitudes 0.2 and 0.3% and an equal number of cycles at the strain amplitude 0.6% compared to the steel studied in [15].

(ii) In the low-nitrogen high-boron 9% Cr steel alloyed with 3% W, 3% Co, 1% Cu, and 0.2% V [20], the number of cycles to failure at 650°C is ~3 times higher at the strain amplitudes 0.2 and 0.3% than that of the studied steel. The short-term strength properties of the steel studied in [20] are generally significantly superior to the properties of the studied steel due to the addition of copper and increased tungsten content.

(iii) In the 10% Cr steel with the closest chemical composition, except for rhenium [12], at the temperature 600°C and strain amplitude 0.2%, the number of cycles to failure is 2 times higher than that of the studied steel, while at the strain amplitude 0.3%, the steel under study demonstrates a two-fold increase, and at the strain amplitude 0.6%, the number of cycles is the same. At 650°C, the steel under study demonstrates an increase in the number of cycles to failure by 20–30%, regardless of the strain amplitude, compared to the steel studied in [12].

Thus, the number of cycles to failure and the degree of softening (~20%) are comparable for the studied 10% Cr steel and similar steels at the test temperatures 600, 650°C and strain amplitudes 0.2, 0.3, 0.6% [12, 15–20]. Structural changes in the new 10% Cr steel due to the modified chemical composition have an insignificant effect on low-cycle fatigue. At both temperatures of 600 and 650°C, no significant increase in the contribution of plastic deformation to the studied steel was observed compared to other 9–10% Cr–3% Co martensitic steels.

CONCLUSIONS

Low-cycle fatigue tests at the temperatures 600, 650°C and strain amplitudes 0.2, 0.3, 0.6, 1% were performed for the new 10% Cr martensitic steel with low nitrogen and high boron. An increase in the strain amplitude significantly reduced the number of cycles to failure. With an increase in the strain amplitude, the plastic components of strain and stress increased. Softening of the material structure was observed from the first test cycles, and the maximum softening was 21% at 600°C and 24% at 650°C in the middle of cyclic loading. It was found that the lath structure of tempered troostite formed during heat treatment underwent significant changes during low-cycle fatigue tests, mainly due to high temperature. The formation of small recrystallized grains was detected, which nucleated at high-angle boundaries, thus increasing the fraction of high-angle boundaries and decreasing the average distance between them. The transformation of the lath structure of tempered troostite into a subgrain structure depended on the strain amplitude. Thus, at low strain amplitudes, the lath structure was predominantly preserved, while the average subgrain size of about 500 nm was comparable with the average width of martensite laths. In contrast, at high strain amplitudes, even with the preservation of lath regions, subgrains with an average size of about 1.2 μm were observed. A decrease in the dislocation density inside laths to 10^{13} m^{-2} was accompanied by shortening of low-angle boundaries of martensite laths, while the dislocation density inside laths remained high (10^{13} m^{-2}). Fractographic analysis showed that, at both test temperatures, numerous crack initiation sites were caused by the formation of oxide particles on the edge of specimens.

ACKNOWLEDGMENTS

The authors are grateful to the Technologies and Materials BelSU Common Use Center for the equipment provided for mechanical testing and structural studies.

FUNDING

The work was financially supported by Russian Science Foundation (agreement No. 19-73-10089-P), https://rscf.ru/project/22-73-41001/.

CONFLICT OF INTEREST

The authors of this work declare that they have no conflicts of interest.

REFERENCES

1. Abe, F., Kern, T.-U., and Viswanathan, R., *Creep-Resistant Steels*, Cambridge: Woodhead Publishing, 2008.
2. Kern, T. U., Staubli, M., Scarlin, B., The European Efforts in Material Development for 650°C USC Power Plants—COST522, *ISIJ Int.*, 2002, vol. 242, pp. 1515–1519. https://doi.org/10.2355/isijinternational.42.1515
3. Fedoseeva, A., Creep Resistance and Structure of 10% Cr–3% Co–2% W–0.29% Cu–0.17% Re Steel with Low Nitrogen and High Boron Contents for Unit Components of Coal Power Plants, *Phys. Mesomech*., 2024, vol. 27, no. 1, pp. 88–101. https://doi.org/10.1134/S1029959924010090
4. Bladesha, H.K.D.H., Design of Ferritic Creep-Resistant Steels, *ISIJ Int.*, 2001, vol. 41, pp. 626–640. https://doi.org/10.2355/isijinternational.41.626
5. Abe, F., Tabuchi, M., and Tsukamoto, S., Alloy Design of MARBN for Boiler and Turbine Applications at 650°C, *Mater. High Temp.*, 2021, vol. 38, pp. 306–321. http://doi.org/10.1080/09603409.2021.1963393
6. Liu, Z., Wang, X., and Dong, C., Effect of Boron on G115 Martensitic Heat Resistant Steel during Aging at 650°C, *Mater. Sci. Eng. A*, 2020, vol. 787, p. 139529. https://doi.org/10.1016/j.msea.2020.139529
7. Zhang, Z., Li, X., Yu, Y., Li, B., Zhang, B., Ma, Y., and Chen, X., Effects of Temperature and Strain Amplitude on Low-Cycle Fatigue Behavior of 12Cr13 Martensitic Stainless Steel, *J. Mater. Res. Technol.*, 2024, vol. 29, pp. 1414– 1427. https://doi.org/10.1016/j.jmrt.2024.01.162
8. Ahiale, G., Choi, W., Cho, S., Park, Y., Chun, Y., and Oh, Y., Low-Cycle Fatigue Behavior of Reduced Activation Ferritic-Martensitic Steel at Elevated Temperatures, *Met. Mater. Int.*, 2023, vol. 29, pp. 71–80. https://doi.org/10.1007/s12540-022-01209-5
9. Shi, S., Li, H., Cui, J., and Chen, X., Impact of Dynamic Strain Aging on Multiaxial Low Cycle Fatigue Behavior of Nickel-Based Alloy 690 at 350°C, *Int. J. Fatig.*, 2023, vol. 170, p. 107547. https://doi.org/10.1016/j.ijfatigue.2023.107547
10. Jauhiainen, P., Yli-Oli, S., Nyholm, A., Auerkari, P., and Salonen, J., Impact of Oxidation on Creep Life of Superheaters and Rehearters, in *Creep & Fracture in High Temperature Components: 2nd ECCC Creep Conference*, 2009, DESTech. Publ., pp. 320–328.
11. Viswanathan, R. and Bakker, W., Materials for Ultrasupercritical Coal Power Plants—Boiler Materials: Part I, *J. Mater. Eng. Perform.*, 2001, vol. 10, pp. 81–95.
12. Mishnev, R., Dudova, N., and Kaibyshev, R., Low Cycle Fatigue Behavior of a 10Cr-2W-Mo-3Co-NbV Steel, *Int. J. Fatigue*, 2016, vol. 83, pp. 344–355.
13. Chauhan, A., Hoffmann, J., Litvinov, D., and Aktaa, J., High-Temperature Low-Cycle Fatigue Behavior of a 9Cr-ODS Steel: Part 1—Pure Fatigue, Microstructure Evolution and Damage Characteristics, *Mater. Sci. Eng. A*, 2017, vol. 707, pp. 207–220. http://dx.doi.org/10.1016/j.msea.2017.09.031
14. Chauhan, A., Hoffmann, J., Litvinov, D., and Aktaa, J., High-Temperature Low-Cycle Fatigue Behavior of a 9Cr-ODS Steel: Part 2—Hold Time Influence, Microstructural Evolution and Damage Characteristics, *Mater. Sci. Eng. A*, 2018, vol. 730, pp. 197–206. https://doi.org/10.1016/j.msea.2018.05.107
15. Zhang, Z., Hu, Z., Schmauder, S., Zhang, B., and Wang, Z., Low Cycle Fatigue Properties and Microstructure of P92 Ferritic-Martensitic Steel at Room Temperature and 873 K, *Mater. Charact.*, 2019, vol. 157, p. 109923.
16. Golanski, G. and Mrozinski, S., Low Cycle Fatigue and Cyclic Softening Behaviour of Martensitic Cast Steel, *Eng. Fail. Analyis,* 2013, vol. 35, pp. 692–702. http://dx.doi.org/10.1016/j.engfailanal.2013.06.019
17. Wang, X., Gong, J., Zhao, Y., Wang, Y., and Yu, M., Characterization of Low Cycle Fatigue Performance of New Ferritic P92 Steel at High Temperature: Effect of Strain Amplitude, *Steel Res. Int.*, 2015, vol. 86, pp. 1046–1055. https://doi.org/10.1002/srin.201400246
18. Wang, X., Zhang, W., Gong, J., and Wahab, M., Low Cycle Fatigue and Creep Fatigue Interaction Behavior of 9Cr-0.5Mo-1.8WV-Nb Heat-Resistant Steel at High Temperature, *J. Nucl. Mater.*, 2018, vol. 505, pp. 73–84. https://doi.org/10.1016/j.jnucmat.2018.03.055
19. Wang, X., Zhang, W., Zhang, T., Gong, J., and Wahab, M., A New Empirical Life Prediction Model for 9–12% Cr Steels under Low Cycle Fatigue and Creep Fatigue Interaction Loadings, *Metals*, 2019, vol. 9, p. 183. https://doi.org/10.3390/met9020183
20. Jing, H., Luo, Z., Xu, L., Zhao, L., and Han, Y., Low Cycle Fatigue Behavior and Microstructure Evolution of a Novel 9Cr–3W–3Co Tempered Martensitic Steel at 650°C, *Mater. Sci. Eng. A*, 2018, vol. 731, pp. 394–402. https://doi.org/10.1016/j.msea.2018.06.071
21. Fedoseeva, A., Nikitin, I., Dudova, N., and Kaibyshev, R., Strain and Temperature Contributions to Structural Evolution in a Re-Containing 10% Cr–3% Co–3% W Steel during Creep, *Mater. High Temp.*, 2021, vol. 38, pp. 237–246. https://doi.org/10.1080/09603409.2021.1924548
22. Fedoseeva, A., Nikitin, I., Dudova, N., and Kaibyshev, R., Superior Creep Resistance of a High-Cr Steel with Re Additives, *Mater. Lett.*, 2020, vol. 262, p. 127183. https://doi.org/10.1016/j.matlet.2019.127183

23. Niessen, F., Apel, D., Danoix, F., Hald, J., and Somers, M.A.J., Evolution of Substructure in Low-Interstitial Martensitic Stainless Steel during Tempering, *Mater. Charact.,* 2020, vol. 167, p. 110494. https://doi.org/10.1016/j.matchar.2020.110494
24. Niessen, F., Gazder, A.A., Hald, J., and Somers, M.A.J., Multiscale In-Situ Studies of Strain-Induced Martensite Formation in Inter-Critically Annealed Extra-Low-Carbon Martensitic Stainless Steel, *Acta Mater.*, 2021, vol. 220, p. 117339. https://doi.org/10.1016/j.actamat.2021.117339
25. Hirsch, P., Direct Observations of Moving Dislocations: Reflections on the Thirtieth Anniversary of the First Recorded Observations of Moving Dislocations by Transmission Electron Microscopy, *Mater. Sci. Eng.,* 1986, vol. 84, pp. 1– 10. https://doi.org/10.1016/0025-5416(86)90216-8
26. Zhilyaev, A., Sergeev, S., and Langdon, T., Electron Backscatter Diffraction (EBSD) Microstructure Evolution in HPT Copper Annealed at a Low Temperature, *J. Mater. Res. Technol.*, 2014, vol. 3, pp. 338–343.
27. Hughes, D. and Hansen, N., Microstructure and Strength of Nickel at Large Strains, *Acta Mater.*, 2000, vol. 48, pp. 2985–3004. https://doi.org/10.1016/S1359-6454(00)00082-3
28. Calcagnotto, M., Ponge, D., Demir, E., and Raabe, D., Orientation Gradients and Geometrically Necessary Dislocations in Ultrafine Grained Dual-Phase Steels Studied by 2D and 3D EBSD, *Mater. Sci. Eng. A*, 2010, vol. 527, pp. 2738–2746. https://doi.org/10.1016/j.msea.2010.01.004
29. Fedoseeva, A., Klauz, A., Raznitsyn, O., and Kaibyshev, R., Creep Strength Breakdown and the Change in Back Stress Strengthening in 10% Cr Martensitic Steels during Creep at 923 K, *Mater. Sci. Eng. A*, 2024, vol. 901, p. 146577. https://doi.org/10.1016/j.msea.2024.146577
30. Fedoseeva, A., Nikitin, I., Dudova, N., and Kaibyshev, R., Nucleation of W-Rich Carbides and Laves Phase in a Re-Containing 10% Cr Steel during Creep at 650°C, *Mater. Charact.*, 2020, vol. 169, p. 110651. https://doi.org/10.1016/j.matchar.2020.110651
31. Kipelova, A., Odnobokova, M., Belyakov, A., and Kaibyshev, R., Effect of Co on Creep Behavior of a P911 Steel, *Metall. Mater. Trans A*, 2013, vol. 44, pp. 577–583. https://doi.org/10.1007/s11661-012-1390-3